# IMPROVED $R_{RS}$ AND TURBIDITY RETRIEVAL FROM OLI IMAGES IN COMPLEX INLAND WATERS: A CASE STUDY FOR LAGUNA DE BAY

M. J. Felix[1] and G. J. Perez[1,2]*

[1]Philippine Space Agency, Quezon City, Philippines - mjbfelix@stamina4space.upd.edu.ph, gay.perez@philsa.gov.ph
[2]Institute of Environmental Science and Meteorology, University of the Philippines Diliman, Quezon City, Philippines - gpperez1@up.edu.ph

**KEY WORDS:** Laguna de Bay, Landsat-8 Operational Land Imager (OLI), remote sensing, turbidity, atmospheric correction.

**ABSTRACT:**

Spatiotemporal monitoring of water quality parameters such as turbidity in inland waters is desirable to better understand productivity and mitigate the negative impacts of pollution induced by increasing anthropogenic activities. However, precise retrieval of water quality parameters in complex turbid waters from the remote sensing reflectance $R_{rs}$, remains a challenging task due to the varying optical complexity of the water body. In this study, a modified version of the Atmospheric Correction for OLI-lite (ModACO) scheme for turbid inland waters, which implements a linear extrapolation of NIR aerosol reflectance in the visible bands instead of a nonlinear function, is presented. The performance of the proposed method and other existing algorithms such as the Atmospheric Correction for OLI-lite (ACOLITE), Management Unit of the Noth Seas Mathematical Models (MUMM) scheme, SeaDAS standard processing, and SWIRE were evaluated. The $R_{rs}$ retrievals from these models were then used as input for turbidity estimation and mapping of Laguna de Bay. Results show lowest $R_{rs}$ error in all five spectral bands (443, 482, 561, 655, and 865 nm) on ModACO-based retrievals. Relative to the ACOLITE and other atmospheric correction schemes, the proposed method reduced the $R_{rs}$ retrieval errors in terms of RMSE and MAPE by more than 50%. Similarly, significant improvements in turbidity retrievals were achieved from ModACO-based $R_{rs}$ values, wherein comparable accuracy was observed from red/green ratio and the single NIR band turbidity models. Turbidity maps of Laguna de Bay show elevated values from the mid of dry season, which may be associated with point source discharge and wind-induced resuspension of bottom sediments. The lake turbidity then drops by the end of dry season, which is linked to the absence of prevailing strong winds that may increase in-water mixing. Using the aforementioned method, accurate monitoring of turbidity can be done to determine and mitigate possible degradation on the water quality of Laguna de Bay and other productive turbid inland waters.

## 1. INTRODUCTION

Turbidity, which refers to clarity of water, is one of the water quality parameters used to evaluate site suitability for aquacultures (Simoes et al., 2008, Tamayo-Zafaralla et al., 2010). It is a dynamic parameter that influences the concentration of dissolved oxygen (DO), chlorophyll-a (chl-a) and surface temperature (ST); parameters that determine the primary productivity (Brown, 1984, Uncles et al., 2017). In freshwater lakes, extended period of high turbidity levels may result to reduced growth and delayed hatching rates among aquatic species (Newcombe and Jensen, 1996). Moreover, high turbidity also increases the cost of water treatment from freshwater bodies used for domestic water supply. Hence, it is essential to monitor the turbidity level in productive inland waters.

While regular $in\ situ$ measurements remains the most accurate method for monitoring water quality, it is based on point observations that may be limited to represent complex and dynamic water systems. Optical satellite remote sensing can provide a comprehensive assessment on the spatial variability of different water quality parameters; information often unavailable with $in\ situ$ measurements. Optical satellites measure the amount of light reflected from water surfaces which carries information about the concentration of different water constituents such as chl-a, suspended solids and colored dissolved organic matter (CDOM) (Hestir et al., 2015, Lymburner et al., 2016). This makes optical remote sensing a valuable tool to measure water quality in a large spatial scale. Among available optical satellites, the Operational Land Imager (OLI) onboard the Landsat-8 has the advantage for coastal and inland water observations given its wide coverage of ∼185 km and spatial resolution of 30 m that can delineate small inland bodies. Moreover, OLI has better signal-to-noise ratio (SNR) compared to its predecessors Thematic Mapper (TM)/Landsat-5 and Enhanced Thematic Mapper Plus (ETM+)/Landsat-7, which improves the reliability of sensor measurements (Irons et al., 2012).

Using semi-empirical and semi-analytical approach, various studies had demonstrated the use of OLI for estimation of different water quality parameters in coastal and inland waters (Lymburner et al., 2016, Braga et al., 2016, Dogliotti et al., 2015, Feng et al., 2012, He and Chen, 2014). The accuracy of these satellite-derived water quality parameters highly depends not only on the empirical/semi-analytical model that relates the apparent optical property (AOP) and concentration of a particular biophysical parameter but also to the atmospheric correction technique implemented to retrieve the AOP often referred as water-leaving or remote sensing reflectance ($R_{rs}$) (Jamet et al., 2011, Dogliotti et al., 2015).

Different atmospheric correction schemes ranging from full physics - based radiative transfer approach to semi-analytical models have been previously used for complex turbid waters such as the SeaDAS standard processing, Atmospheric Correction for OLI-lite (ACOLITE), ShortWave Infrared Extrapolation (SWIRE), and Management Unit of the North Seas Mathematical Models (MUMM) algorithm (Franz et al., 2015, He and Chen, 2014,

* Corresponding author

Vanhellemont and Ruddick, 2014, Vanhellemont and Ruddick, 2015, Jamet et al., 2011). The SeaDAS standard processing implements the black pixel approximation which assumes a negligible water-leaving reflectance on the NIR and SWIR bands. The spectral ratio of two NIR or SWIR bands is used to determine the appropriate model for extrapolation of aerosol reflectance in the visible bands. Lastly, an iterative model was employed to reduce the error in the calculated spectral ratio due to non-zero water-leaving NIR reflectance in turbid waters. The MUMM algorithm is mainly based on two assumptions. First, the ratio of two NIR or red water-leaving reflectance is assumed to be constant. Second, the spatial distribution of atmospheric aerosol in the area of interest is considered homogeneous. The ACOLITE and SWIRE algorithm utilize the SWIR bands, wherein the water-leaving reflectance is considerably negligible, for aerosol estimation. The ACOLITE algorithm uses a power function to extrapolate the aerosol contribution in the visible bands, whereas, the SWIRE technique employs an exponential model. The efficacy of these algorithms have been proven in previous studies, however, the respective accuracy of these models largely varies in complex turbid inland waters due to several factors such as high aerosol optical depth (AOD), high backscattering from total suspended solids (TSS) and high concentration of colored dissolved organic matter (CDOM) (Feng et al., 2012).

The main objective of this study is to reduce the errors associated with $R_{rs}$ retrieval in complex and turbid inland waters, consequently improving the accuracy of derived water quality parameters such as turbidity. This is demonstrated by introducing some modifications in the ACOLITE algorithm. By using an empirically-derived function to estimate the NIR aerosol reflectance along with a linear extrapolation in the visible bands, improvement in the accuracy $R_{rs}$ retrieval is achieved. Along with the other atmospheric correction schemes, the accuracy of the modified ACOLITE (ModACO) algorithm was evaluated for $R_{rs}$ and turbidity retrieval in the complex waters of Laguna de Bay.

## 2. DATA

### 2.1 Study Site and Field Data Collection

Laguna de Bay is the largest lake in the Philippines with a total area of $\sim$900 $km^2$. It is a eutrophic and shallow lake with an average depth of $\sim$ 2.8 $m$. The lake has been widely used for fish production, irrigation and domestic water supply (Barril and Tumlos, 2002). Due to the rapid growth in population and industrial activities, the lake becomes more vulnerable to water pollution. From 1986 to 1995, a decreasing trend in water clarity was observed, which may be an indicator of water quality degradation (Barril and Tumlos, 2002). If not addressed accordingly, this may cause water-related health problems on nearby communities and significant loss in fish production.

Optical measurements were conducted at a total of 45 sites within Laguna de Bay. These data were acquired from April 23-24, 2018, April 4-7 and April 19-20 2017. The location of sampling sites are shown in Figure 1. Turbidity and spectral measurements were taken using the Horiba multiparameter water quality sensor and ASD FieldSpec 4 spectroradiometer, respectively. The $R_{rs}$ was computed using equation 1,

$$R_{rs}(\lambda) = \frac{L_{sw}(\lambda) - [r_{sky} \cdot L_{sky}(\lambda)]}{E_d(\lambda)} \quad (1)$$

where $L_{sw}$ denotes the upwelling radiance above the water surface, $E_d$ is the downwelling irradiance just above the water surface, $L_{sky}$ is the sky radiance and $r_{sky}$ is the Fresnel reflectance of skylight at air-water boundary set at 0.022 (Dorji and Fearns, 2017). The value of $r_{sky}$ can range from 0.022 to 0.027 depending on the wind speed. To remove residual reflectance possibly due to glint, the mean reflectance from 1200-1250 nm was subtracted to equation 1.

### 2.2 Derivation of Turbidity Models

To match and validate the $R_{rs}$ values retrieved from OLI, band averaging of ground hyperspectral data was carried out. The band-weighted $R_{rs}$ values were calculated using equation 2,

$$< R_{rs}(\lambda) >= \frac{\int R_{rs}(\lambda) \cdot RSRF(\lambda) \cdot d\lambda}{\int RSRF(\lambda) \cdot d\lambda} \quad (2)$$

where $RSRF$ denotes the relative spectral response function of OLI at different bands and $< R_{rs} >$ is the band-averaged reflectance. From here on, $< R_{rs} >$ will be referred as $R_{rs}$ for brevity. Turbidity models were then derived via correlation analysis of turbidity and $R_{rs}$ at specific bands. The green (band 3), red (band 4), NIR (band 5) channel of OLI and corresponding band ratios were used to estimate the turbidity in Laguna de Bay. The number of turbidity models were then filtered based on the resulting coefficient of determination ($R^2$) from the correlation analysis. Turbidity models with ($R^2 > 0.9$) are only considered as shown in equations 3-5,

$$T = [21252 \cdot R_{rs}(865)] + 4.08 \quad , R^2 = 0.94 \quad (3)$$

$$ln(T) = \left[3.7003 \cdot ln\left(\frac{R_{rs}(655)}{R_{rs}(561)}\right)\right] + 5.47 \quad , R^2 = 0.97 \quad (4)$$

$$ln(T) = \left[1.307 \cdot ln\left(\frac{R_{rs}(865)}{R_{rs}(655)}\right)\right] + 6.68 \quad , R^2 = 0.92 \quad (5)$$

where $T$ denotes the turbidity value in nephelometric turbidity unit ($NTU$). The sample size $n$ used in the correlation analysis is 22. Note that different datasets were used in the calibration and validation of turbidity models.

## 3. METHODS

### 3.1 Atmospheric Correction using the ModACO Algorithm

#### 3.1.1 Calculation of the Top-of-Atmosphere TOA reflectance $\rho_{TOA}$ from OLI Images //

OLI images of Laguna de Bay acquired from March to May 2017 and April 23, 2018 were used in this study. These images were downloaded from the United States Geological Survey Earth Explorer website $https://earthexplorer.usgs.gov/$

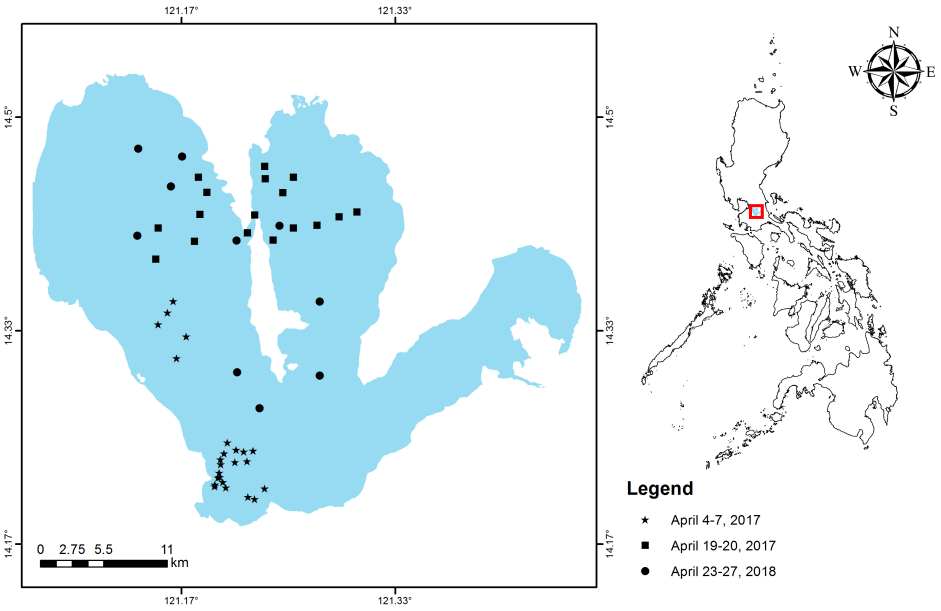


Figure 1. Map of the Philippines (right) and the distribution of sampling sites across the South, West and Central Bay of Laguna de Bay (left).

. The downloaded datasets include orthorectified images in Digital Number (DN) and a supporting metadata file. The images in Digital Number (DN) were then converted to top-of-atmosphere radiance $L_{TOA}$ using equation 6,

$$L_{TOA} = (M_L \cdot DN_{TOA}) + A_L \tag{6}$$

where $DN_{TOA}$ is the pixel value in DN, $M_L$ and $A_L$ is the multiplicative and additive factor, respectively. The $M_L$ and $A_L$ are both provided in the metadata file. Note that $L_{TOA}$ is wavelength dependent. The symbol $\lambda$ was omitted for brevity. The TOA radiance was then converted to reflectance using equation 7,

$$\rho_{TOA} = \frac{\pi \cdot d^2 \cdot L_{TOA}}{ESI \cdot cos\theta_0} \tag{7}$$

where $d$ is the sun-earth distance correction factor, $ESI$ is the band-averaged extraterrestrial solar irradiance and $\theta_0$ is the solar zenith angle.

The TOA reflectance can then be decomposed to several components as given by equation 8,

$$\rho_{TOA} = \rho_{Ray} + \rho_a + \rho_{r-a} + T\rho_g + t(\rho_w + \rho_{wc}) \tag{8}$$

where $\rho_w$ is the the water-leaving reflectance, $\rho_{Ray}$ is the contribution from Rayleigh scattering, $\rho_a$ is the aerosol scattering, $\rho_{r-a}$ is the interaction between aerosol and Rayleigh scattering, $\rho_g$ is the specular reflectance of sunlight from the air-water interface and $\rho_{wc}$ is the reflectance from whitecaps (Franz et al., 2015, Pahlevan et al., 2017a). The symbols $t$ and $T$ denotes the two-way diffuse and direct transmittance, respectively. The aim of atmospheric correction is to retrieve the water-leaving reflectance and effectively $R_{rs}$ defined by equation 9.

$$R_{rs} = \rho_w/\pi \tag{9}$$

Similar to the ACOLITE algorithm, the ModACO implements the single scattering approximation wherein $\rho_{r-a}$ is assumed to be included in the calculation of $\rho_a$ (Dash et al., 2012, Vanhellemont and Ruddick, 2014). Also, the contribution from $\rho_{wc}$ is assumed to be negligible and largely compensated in the $\rho_a$ computation. At conditions where the solar zenith angle $\theta_0$ is much larger than the sensor zenith angle $\theta_v$, the contribution from $\rho_g$ can be ignored. Hence, equation 8 is reduced to equation 10.

$$\rho_{TOA} = \rho_{Ray} + \rho_a + t\rho_w \tag{10}$$

#### 3.1.2 Calculation of the Rayleigh reflectance $\rho_{Ray}$ //

The Rayleigh reflectance $\rho_{Ray}$ is given by equation 11,

$$\rho_{Ray} = \frac{\tau_r \cdot P_r}{4cos\theta_0 \cdot cos\theta_v} \tag{11}$$

where $\tau_r$ is Rayleigh optical thickness and the Rayleigh scattering phase function $P_r$ is defined as,

$$P_r = P_r(\theta_-) + P_r(\theta_+)[r(\theta_v) + r(\theta_0)] \tag{12}$$

and $P_r(\theta_\pm)$ is given as,

$$P_r(\theta_\pm) = 0.75(1 + cos^2\theta_\pm) \tag{13}$$

The subscripts $+$ and $-$ denotes the Rayleigh contribution from direct scattering and scattered light interacting with air-sea surface. The scattering angles are computed using equation 14,

$$cos\theta_{\pm} = \pm cos\theta_0 cos\theta_v - sin\theta_0 sin\theta_v cos|\Delta\phi| \quad (14)$$

where $\Delta\phi$ denotes the relative azimuth angle. The Fresnel reflection coefficient for unpolarized light $r(\theta)$ is given by equation 15,

$$r(\theta_i) = 0.5\left[\frac{sin^2(\theta_i - \theta_j)}{sin^2(\theta_i - \theta_j)} + \frac{tan^2(\theta_i - \theta_j)}{tan^2(\theta_i - \theta_j)}\right] \quad (15)$$

where $\theta_i$ is equal to $\theta_0$ for $r(\theta_0)$ and $\theta_v$ for $r(\theta_v)$ calculation. The angle $\theta_j$ is computed using the Snell's law given by equation 16,

$$n = sin\theta_i / sin\theta_j \quad (16)$$

and $n$ is the refractive index of water taken as 1.333.

The Rayleigh-corrected reflectance $\rho_{rc}$ is defined by equation 17

$$\rho_{rc} = \rho_{TOA} - \rho_{Ray} \quad (17)$$

#### 3.1.3 Estimation of aerosol reflectance $\rho_a$ and $R_{rs}$ retrieval //

The aerosol correction of the ModACO algorithm begins with the estimation of $\rho_a(865)$ from the linear extrapolation of Rayle-igh-corrected SWIR bands wherein the water-leaving reflectance is considerably negligible. The next step then includes the extrapolation of the aerosol values from the NIR band to the visible bands. With the SWIRE and ACOLITE algorithm, this was done using an exponential and power function based on Rayleigh -corrected SWIR bands. However, this approach tends to overestimate the aerosol reflectance in complex inland waters commonly characterized with high AOD and turbidity values. In this study, the extrapolation to visible bands (443, 482 and 561 nm) was conducted only after the aerosol reflectance at red band $\rho_a(655)$ was estimated. The $\rho_a(655)$ was estimated as a function of $\rho_a(865)$ as given by equation 18

$$\rho_a(655) = m_e(655 - 865) + \rho_a(865) \quad (18)$$

where $m_e$ is given by equation 19),

$$m_e = \frac{\rho_a(865) - \delta}{800} \quad (19)$$

where the aerosol parameter $\delta$ was determined from the Rayleigh -corrected NIR reflectance $\rho_{rc}(865)$ of cloud-free clear water pixels, where the slope between $\rho_{rc}(865)$ and to $\rho_{rc}(655)$ is nearly zero. In this study, the value of $\delta$ is found to be approximately equal to 0.043. The aerosol reflectance at green and blue bands were then extrapolated using equation 20,

$$\rho_a(\lambda) = \rho_a(865) \cdot \left[\frac{\rho_a(655)}{\rho_a(865)}\right]^{\beta(\lambda)} \quad (20)$$

where $\beta$ is defined as,

$$\beta(\lambda) = \frac{865 - \lambda}{865 - 655} \quad (21)$$

The remote sensing reflectance of visible bands can now be calculated using equations 9 and 10. Lastly, the water-leaving reflectance at NIR band $\rho_w(865)$ was computed using the turbidity models described by equations 3 and 4 wherein $\rho_w(865)$ can be calculated as a function of $\rho_w(561)$ and $\rho_w(655)$ . The summary of the ModACO algorithm is as follows:

1. Calculate for the Rayleigh-corrected reflectances $\rho_{rc}(\lambda)$.
2. Calculate $\rho_a(865)$ from the linear extrapolation of Rayleigh-corrected SWIR bands.
3. Calculate $\rho_a(655)$ using equations 18 and 19.
4. Estimate the aerosol reflectance at blue and green bands using the power function given by equation 20
5. Calculate for the remote sensing reflectance of visible bands using equations 9 and 10.
6. Finally, calculate $R_{rs}(865)$ using equations 3 and 4.

### 3.2 Implementation of Other Atmospheric Correction Algorithms

Atmospheric correction schemes for turbid waters such as the SeaDAS standard processing, ACOLITE, SWIRE and MUMM algorithm were also employed and evaluated. The SeaDAS standard processing utilizes the 865 and 1609 nm band to calculate for the aerosol parameter $\epsilon$ which is used to determine the aerosol model for extrapolation at visible bands. Furthermore, it implements an iterative approach to compensate for the nonzero $\rho_w$ at NIR band. The ACOLITE and SWIRE algorithm utilize the SWIR bands to extrapolate the aerosol reflectance in visible bands using a power and exponential function, respectively. The MUMM algorithm is implemented in the SeaDAS platform wherein the marine reflectance ratio $\alpha$ is set to 8.702 and the aerosol ratio $\epsilon$ and two-way transmittance $\gamma$ set to unity. Note that vicarious calibration coefficients were used in the implementation of all atmospheric algorithms (Pahlevan et al., 2017b).

### 3.3 Accuracy Assessment

The performance of the propose method is compared with other existing atmospheric correction algorithms for turbid waters such as the SeaDAS standard processing, ACOLITE, SWIRE and MUMM algorithm. The metrics used for accuracy assessment of satellite-derived $R_{rs}$ and turbidity include the root mean square error (RMSE) and mean absolute percent error (MAPE) as given by equations 22 and 23, respectively

$$RMSE = \sqrt{\frac{1}{n}\sum_{i=1}^{n}(y_i - y_i')^2} \quad (22)$$

$$MAPE = \frac{1}{n}\sum_{i=1}^{n}\left|\frac{y_i - y_i'}{y_i}\right| \quad (23)$$

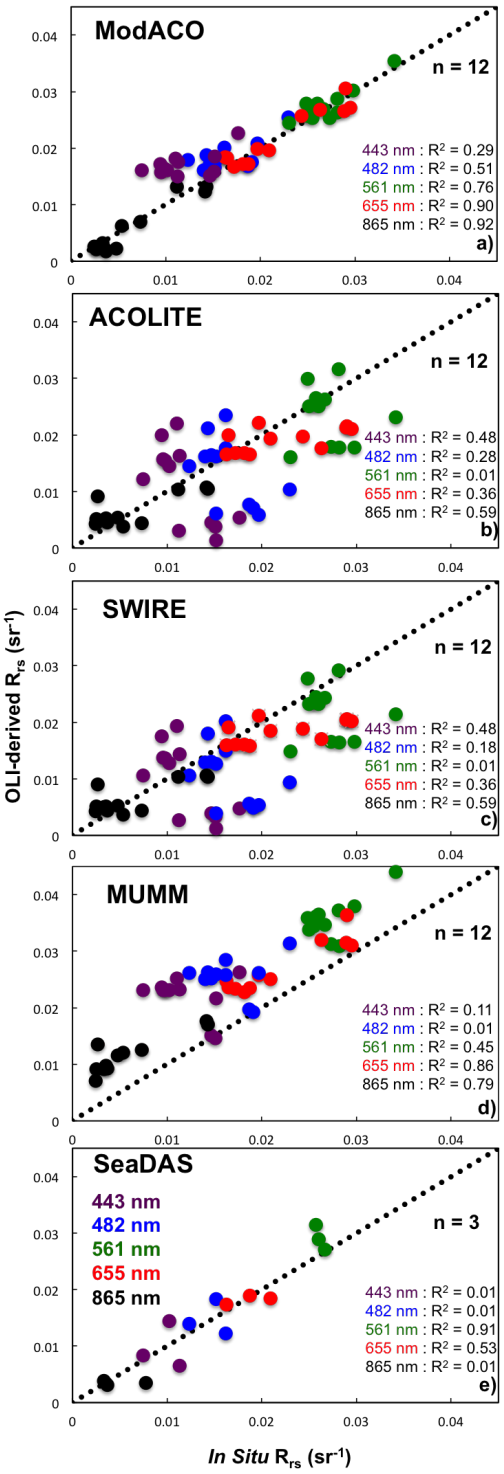


Figure 2. Correlation plots of $in\ situ$ and OLI-derived $R_{rs}$ values using different atmospheric correction schemes. The SeaDAS standard processing only yield valid $R_{rs}$ values on April 20, 2017 image. The dotted line pertains to the 1:1 correspondence.

where $y_i$ and $y_i'$ denotes the $in\ situ$ and satellite-derived measurement, respectively. Note that $3x3$ pixel averaging and a temporal coincidence of $\pm 5$ hr was defined for the validation of OLI-derived measurements.

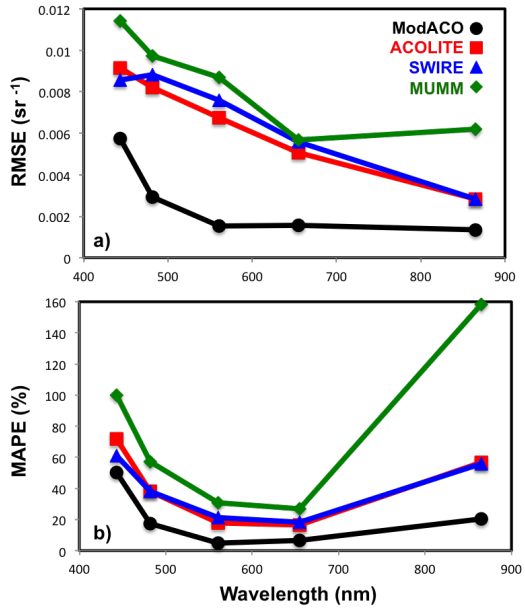


Figure 3. The accuracy in terms of RMSE and MAPE of different atmospheric correction schemes at the NIR and visible bands.

## 4. RESULTS AND DISCUSSION

### 4.1 $R_{rs}$ Retrieval

The correlation plots of in situ and satellite $R_{rs}$ derived using different atmospheric correction schemes are shown in Figure 2. Good correspondence between $in\ situ$ and ModACO-derived $R_{rs}$ values can be observed as evident from clustered scatter points along the 1:1 line. Contrastingly, overestimated $R_{rs}$ values were obtained from MUMM algorithm, which is indicated by scatter points above the 1:1 line. Closely identical correlation plots characterized by sparsely distributed points along the 1:1 line can be observed from SWIRE and ACOLITE algorithm. No coincident $R_{rs}$ values were retrieved from April 04, 2017 and April 23, 2018 OLI images using the standard SeaDAS processing, which results to inadequate number of correlation points. Hence, accuracy assessment was conducted only on ModACO, SWIRE, ACOLITE and MUMM algorithm. The corresponding accuracy of each algorithm at five spectral bands is shown in Figure 3. The ModACO and MUMM algorithm yields the most and least accurate $R_{rs}$ retrieval in all spectral bands, respectively. As expected, closely similar accuracies between SWIRE and ACOLITE were observed. The ModACO algorithm yields the least errors in the longer wavelengths (561 - 865 nm), which increases on the blue bands (443 and 482 nm).

The success in $R_{rs}$ retrieval of ModACO in complex turbid inland waters is highly dependent on two factors: i) estimation of NIR aerosol reflectance and ii) its extrapolation on visible bands. With the use of SWIR bands, a fairly accurate estimate of NIR aerosol reflectance can be achieved. Unlike the SWIRE and ACOLITE algorithm which employs an exponential and power function extrapolation to estimate $\rho_a(865)$, respectively, a linear extrapolation was found to be more suitable. After $\rho_a(865)$ was estimated, the appropriate aerosol extrapolation model was determined using equation 19. The determination of the aerosol model in ModACO is mainly dependent on the estimated $\rho_a(865)$ which is direcly related on the AOD. At high AOD vaues, the slope between $\rho_a(655)$ and $\rho_a(865)$

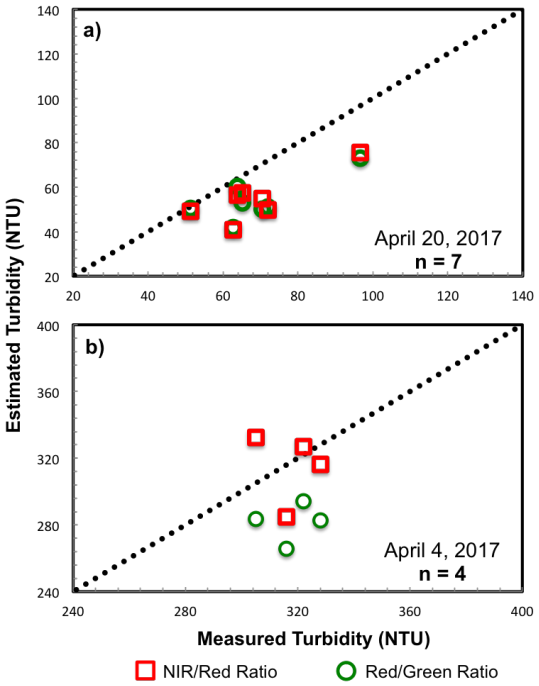


Figure 4. Correlation plots of $in\ situ$ and OLI-derived turbidity using $R_{rs}$ values derived from the ModACO scheme. The 1:1 line is denoted by the black dots.

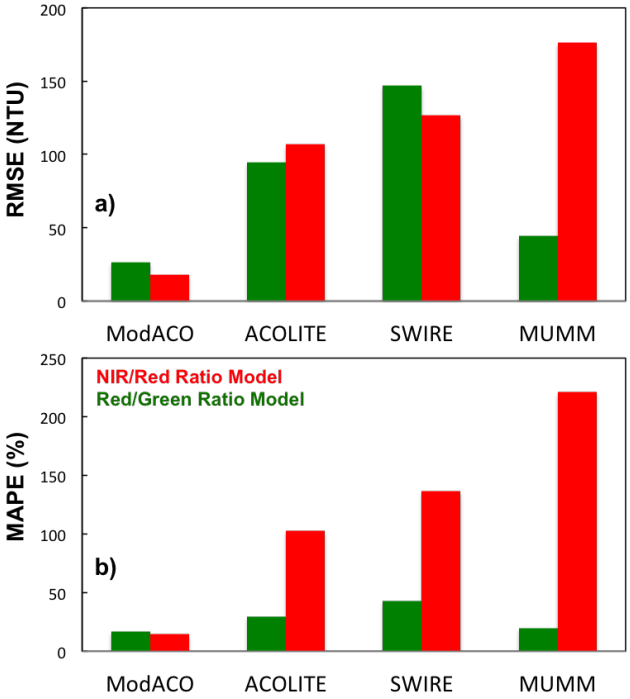


Figure 5. The accuracy of turbidity models based on $R_{rs}$ values derived different atmospheric correction methods.

may be nearly zero or even positive. This dynamic change in aerosol model based on AOD values is accounted in the ModACO as decribed by equation 19. The ModACO algorithm yield accurate $R_{rs}$ retrievals in red to blue bands (482, 561 and 655 nm) with an apparent overestimation in the deep blue band (443 nm). This indicates that the aerosol model underestimates in shorter wavelengths where the aerosol scattering is relatively high. However, it can be observed from Figure 2 that the scatter plot of $R_{rs}(443)$ has similar slope with the 1:1 line. This suggests that a bias correction or a scaling factor may be applied to improve the retrieval in this band. Lastly, $\rho_w(865)$ was estimated using an algebraic manipulation of turbidity models described by equations 3 and 4, rather than directly computing equation 10 with the initial estimate of $\rho_a(865)$. This is based on the fact that the initial estimate of $\rho_a(865)$ may be influenced by whitecaps, glint and signal from adjacent land pixels, which has a more significant impact on the calculation of water-leaving reflectance in NIR compared to visible bands. Furthermore, the use of equations 3 and 4 removes the dependence on the actual turbidity and predicts $\rho_w(865)$ only from the spectral ratio of $\rho_w(561)$ and $\rho_(655)$.

### 4.2 Turbidity Retrieval

The $R_{rs}$ retrieval failure of the SeaDAS standard processing on several pixels is attributed to invalid range of calculated $\epsilon$ values used to determine the appropriate aerosol models (Pahlevan et al., 2017a). This commonly occurs at turbid waters with high AOD condition. At such conditions o, the SWIRE and ACOLITE algorithm was also found to have excessive aerosol retrieval resulting to underestimated $R_{rs}$ values. In general, the SeaDAS, SWIRE and ACOLITE algorithms only yield relatively accurate retrievals on April 20,2017 image, which is characterized with low turbidity (30 - 120 $NTU$) and $AOD_{865}$ (0 - 0.1). The overestimation of the MUMM algorithm may be associated with the simplification of the two-way transmittance $\gamma$ and aerosol ratio $\epsilon$ to unity, which does not account the sun-sensor orientation and meteorological variation in every scene.

Figure 4 shows the accuracy of two turbidity models based on ModACO-derived $R_{rs}$ values. Generally, good turbidity estimates were obtained from the models. Both models underestimate on April 20, 2017 image, which is characterized with low turbidity values. On April 04, 2017 image, the NIR/red model described by equation 5 yields more accurate retrieval compared to the red/green model which slightly underestimates the turbidity values. Comparison of turbidity estimates based on the $R_{rs}$ values derived from other atmospheric correction scheme was also conducted as shown in Figure 5. ModACO-based retrieval yield the most accurate turbidity values regardless of the model used. Based on corresponding MAPE, the NIR/red model achieved better results in in ModACO, whereas, the red/green model yield more accurate results for the other remaining atmospheric correction methods. Interestingly, the MUMM (red/green) turbidity model yield comparable accuracy with ModACO despite having the highest $R_{rs}$ retrieval errors.

It is known that the uncertainties in the atmospheric correction process propagate to higher-level remote sensing products such as turbidity. However, the impact of $R_{rs}$ retrieval errors can be reduced with the use of models based on spectral band ratios, as evident from the MUMM red/green ratio turbidity model. Though overestimated $R_{rs}$ values were generally obtained from the MUMM algorithm, it was able to retain the spectral relationship between the red and green band, yielding comparable accuracy with ModACO-based turbidity models. In fact, the slope of correlation points from MUMM algorithm in the NIR, red and green band matches that of the 1:1 line as observed in Figure 2. This suggests that a bias correction may be implemented on these bands to improve the correspondence with $in\ situ$ values. However, this approach warrants more datasets for calibration and validation. Nonetheless, this result showed

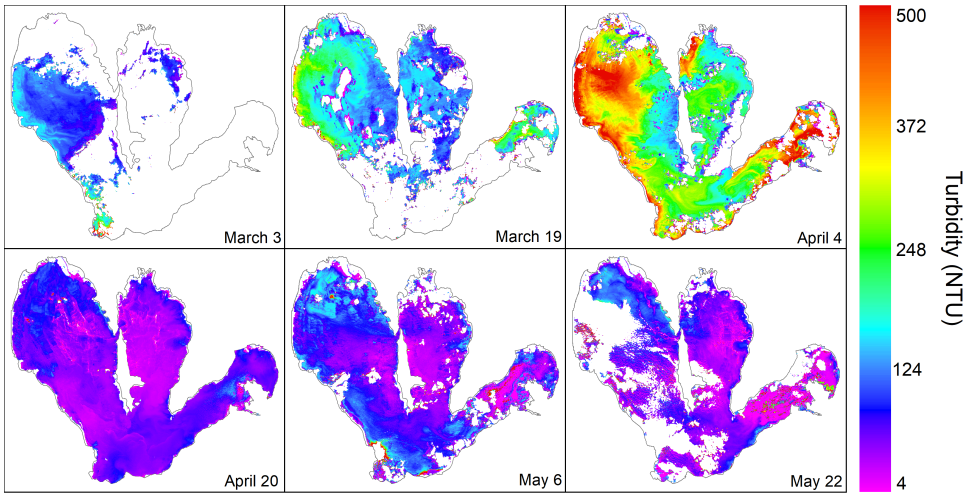


Figure 6. Turbidity maps of Laguna de Bay during the dry season of 2017. Note that the areas without turbidity retrieval correspond to cloud-covered pixels.

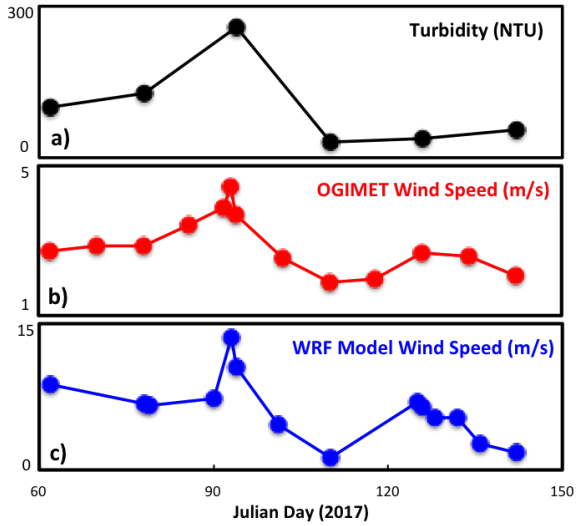


Figure 7. Temporal variability of turbidity and wind speed in Laguna de Bay. Wind data were acquired from NOAH-WISE Weather Research Forecast (WRF) Model and OGIMET synoptic stations. Note that the wind data from four synoptic stations that surround Laguna de Bay (Tayabas, Tanay, Ambulong and NAIA) were averaged, whereas, the data shown from NOAH-WISE corresponds to the modeled wind at the central Bay.

the advantage of spectral band ratio for turbidity retrieval.

### 4.3 Mapping Using ModACO-based Turbidity Model

Using ModACO-based turbidity models, particularly the NIR/red ratio, monitoring of Laguna de Bay using OLI images may be conducted. To demonstrate, turbidity maps of Laguna de Bay from March to May of 2017 were generated. These maps are shown in Figure 6. It can be seen that the turbidity of the lake increases from March 3 and peaks at April 4. A significant drop in turbidity was then observed from April 20 until the end of the dry season. The increase in lake turbidity from March 3 to April 4 may be attributed to different factors such as lake hydrodynamics, effluence from points sources and resuspension of lake bed sediments (Luettich Jr. et al., 1990, Herrera et al., 2015).

During the dry season, counter-clockwise circulations that converge on the northwest portion of the lake are prevalent (Cunanan and Salvacion, 2016, Herrera et al., 2015). These converging currents may cause the transport of sediments resulting to elevated values on the northwest portion of the bay as observed on April 20, May 6, and May 22 turbidity maps. Discharge from point sources such as factories, water treatment facilities and agricultural run-off may also increase the water turbidity through the addition of colored effluent and suspended solids. However, the increase in turbidity from point source discharge is commonly localized and may not account for the elevated turbidity across the lake on April 4. On the contrary, resuspension of bed sediments, depending on the mechanism, may be observed on a small or larger spatial scale. Bed sediments may be agitated or stirred up by bottom-feeder/dweller fishes resulting to localized resuspension (Yahel et al., 2002, Scheffer et al., 2003). Such phenomenon may have caused the relatively high turbidity measurements on several fish pens located on the northern part of West Bay on May 6. This occurrence is highly probable on similar areas in the lake characterized with shallow depth and high fish density. On the contrary, wind-induced resuspension of bottom sediments may result to elevated turbidity across the lake. Persisting strong winds generate large surface waves thereby increasing the effective bed shear stress. When the critical bed shear stress is exceeded, resuspension of lake bed sediments occurs (Luettich Jr. et al., 1990, Valipour et al., 2017). This mechanism may explain the high turbidity values across the lake on April 4. As shown in Figure 7, the averaged wind speed observed from the WRF model and OGIMET synoptic stations peaks at April 3 (OGIMET, 2018, Combinido and Perez, 2014). Strong winds coming from the eastern side persist on April 4, the same day the lake turbidity reached its maximum. Moreover, the effect of strong westward winds on the water movement is evident on the West Bay wherein a gradient in turbidity can be observed from the east to the west side of the bay. The gradient in turbidity is related to the increase in fetch as the wind traverse westward. This results to higher bed shear stress towards the west side of the lake thereby increasing the concentration of resuspended bottom sediments.

The decline in turbidity values at the end of dry season may be associated with the settling of suspended sediments due to the lack of persisting strong winds that may induce continuous mixing in the water column. This period coincided with the intermonsoon break wherein no prevailing wind is present (Botin

et al., 2010, Ooi et al., 2017). The lake turbidity may also drop rapidly at the event of salt water intrusion as salt ions tend to aggregate suspended particles and thereby increasing their settling velocity (Hakanson, 2006, Santiago, 1991). Such occurrence is commonly observed at the end of dry season when the the water level of the lake dips at minimum. Salt water from Manila Bay mainly pass through the Pasig river and eventually reach Laguna de Bay through the Napindan channel (Santiago, 1991).

## 5. SUMMARY AND CONCLUSION

In this study, an improved atmospheric correction method based on the ModACO scheme was demonstrated on the turbid waters of Laguna de Bay. Advantages of the proposed method include: (1) accurate retrieval at turbid waters with high AOD, conditions where most algorithms fail or are inaccurate and (2) relatively simple and adaptive algorithm. However, the model is expected to have lower accuracies at shorter wavelengths where the actual spectral aerosol reflectance may deviate significantly. This may be mitigated using a bias correction or scaling factor which warrants additional datasets. Furthermore, it will be valuable to test the accuracy of ModACO in other complex turbid waters where the composition of atmospheric aerosol and optically active water constituents may differ from that of Laguna de Bay.

The accuracy of the ModACO algorithm is reflected on the turbidity retrieval, wherein ModACO-based turbidity models yield the least errors among the evaluated atmospheric correction schemes. The MoDACO NIR/red model was then used to determine the spatiotemporal changes in turbidity from March to May 2017 in Laguna de Bay. Results show strong correlation between turbidity and wind speed, suggesting the occurrence of wind-induced resuspension of bottom sediments in the lake on strong wind conditions, e.g., on April 4, 2017. For future studies, profiling of bathymetry and bed sediment sizes in the lake is recommended to accurately model the spatiotemporal distribution of turbidity and TSS across the lake at various wind conditions.

## ACKNOWLEDGMENTS

This work was supported by the Department of Science and Technology (DOST) under the Remote Sensing Product Development of Stamina4Space Program. The authors would like to thank E.M. Leonardo, L.A. Fulgencio, J. Madalipay, E. Quiambao, R. J. Goliat, S. Namuco, and F. M. Felicio for their help in the collection and processing of $in\ situ$ measurements. The authors would like also to thank H. Merida for the layout of GIS maps.

## REFERENCES

Barril, C. R., Tumlos, E. T., 2002. Water quality trends and trophic state assessment of Laguna de Bay, Philippines. *Aquatic Ecosystem Health*, 5(2), 115–126.

Botin, Z. T., David, L. T., del Rosario, R. C. H., Parrott, L., 2010. Spatio-Temporal Complexity analysis of the Sea Surface Temperature in the Philippines. *Ocean Science*, 6, 933–947.

Braga, F., Zaggia, L., Bellafiore, D., Bresciani, M., Giardino, C., Lorenzetti, G., Maicu, F., Manzo, C., Riminucci, F., Ravaioli, M., Brando, V. E., 2016. Mapping turbidity patterns in the Po river prodelta using multi-temporal Landsat 8 imagery. *Estuarine, Coastal and Shelf Science*, 198, 555–567.

Brown, R., 1984. Relationships between suspended solids, turbidity, light attenuation and algal productivity. *Lake and Reservoir Management*, 1(1), 198–205.

Combinido, J. S., Perez, G. J., 2014. Impact of tagaytay doppler radar assimilation on wrf rainfall prediction. *Proc. 32nd SPP Congress*.

Cunanan, A., Salvacion, J., 2016. Hydrodynamic Modeling of Laguna Lake Using Environmental Fluid Dynamics Code. *International Journal of Research in Chemical, Metallurgical and Civil Engineering*, 3(1), 21–26.

Dash, P., Walker, N., Mishra, D., D'Sa, E., Ladner, S., 2012. Atmospheric Correction and Vicarious Calibration of Oceansat-1 Ocean Color Monitor (OCM) Data in Coastal Case 2 Waters. *Remote Sensing*, 4, 1716–1740.

Dogliotti, A. I., Ruddick, K. G., Nechad, B., Doxaran, D., Knaeps, E., 2015. A single algorithm to retrieve turbidity from remotely-sensed data in all coastal and estuarine waters. *Remote Sensing of the Environment*, 156, 157–168.

Dorji, P., Fearns, P., 2017. Impact of the spatial resolution of satellite remote sensing sensors in the quantification of total suspended sediment concentration: A case study in turbid waters of Northern Western Australia. *Plos ONE*, 12(4), 1–24.

Feng, L., Hu, C. M., Chen, X. L., Tian, L. Q., Chen, L. Q., 2012. Human induced turbidity changes in Poyang Lake between 2000 and 2010: Observations from MODIS. *Journal of Geophysical Research*, 117(C7), 1–19.

Franz, B. A., Bailey, S. W., Kuring, N., Werdell, P. J., 2015. Ocean color measurements with the Operational Land Imager on Landsat-8: implementation and evaluation in SeaDAS. *Journal of Applied Remote Sensing*, 9(1), 157–168.

Hakanson, L., 2006. The relationship between salinity, suspended particulate matter and water clarity in aquatic systems. *Ecological Research*, 21(1), 75–90.

He, Q., Chen, C., 2014. A new approach for atmospheric correction of MODIS imagery in turbid coastal waters: a case study for the Pearl River Estuary. *IEEE Journal of Selected Topics in Applied Earth Observation*, 5(3), 249–257.

Herrera, E., Nadaoka, K. Blanco, A. C., Hernandez, E., 2015. Hydrodynamic investigation of a shallow tropical lake environment (Laguna Lake, Philippines) and associated implications for eutrophic vulnerability. *ASEAN Journal of Chemical Engineering*, 4, 48–63.

Hestir, E. L., Brando, V. E., Bresciani, M., Giardino, C., Matta, E., Villa, P., Dekker, A. G., 2015. Measuring freshwater aquatic ecosystems: The need for a hyperspectral global mapping satellite mission. *Remote Sensing of the Environment*, 167(15), 181–195.

Irons, J. R., Dwyer, J. L., Barsi, J. A., 2012. The next Landsat satellite: The Landsat Data Continuity Mission. *Remote Sensing of the Environment*, 122, 11–21.

Jamet, C., Loisel, H., Kuchinke, C. P., Ruddick, K., Zibordi, G., Feng, H., 2011. Comparison of three SeaWiFS atmospheric correction algorithms for turbid waters using AERONET-OC measurements. *Remote Sensing of the Environment*, 155, 1955–1965.

Luettich Jr., R. A., D. Harleman, R. F., Somlyody, L., 1990. Dynamic behavior of suspended sediment concentrations in a shallow lake perturbed by episodic wind events. *Limnology and Oceanography*, 35(5), 1050–1067.

Lymburner, L., Botha, E., Hestir, E., Anstee, J., Sagar, S., Dekker, A., Malthus, T., 2016. Landsat 8: Providing continuity and increased precision for measuring multi-decadal time series of total suspended matter. *Remote Sensing of the Environment*, 185, 108–118.

Newcombe, C. P., Jensen, J. O. T., 1996. Channel Suspended Sediment and Fisheries: A Synthesis for Quantitative Assessment of Risk and Impact. *North American Journal of Fisheries Management*, 16(4), 694–727.

OGIMET, 2018. OGIMET. [Online]. Available: http://ogimet.com/gsodc.phtml.en.

Ooi, M. C. G., Chan, A., Subramaniam, K., Morris, K. I., Oozeer, M. Y., 2017. Interaction of urban heating and local winds during the calm intermonsoon seasons in the tropics. *Journal of Geophysical Research: Atmospheres*, 122(21), 499–523.

Pahlevan, N., Roger, J., Ahmad, Z., 2017a. Revisiting short-wave-infrared (SWIR) bands for atmospheric correction in coastal waters. *Optics Express*, 25(6), 6015–6035.

Pahlevan, N., Schott, J. R., Franz, B. A., Zibordi, G., Markham, B., Bailey, S., Schaaf, C. B., Ondrusek, M., Greb, S., Strait, C. M., 2017b. Landsat 8 remote sensing reflectance (Rrs) products: Evaluations, intercomparisons, and enhancements. *Remote Sensing of the Environment*, 190, 289–301.

Santiago, A. E., 1991. Turbidity and seawater intrusion in Laguna de Bay. *Environmental Monitoring and Assessment*, 16(1), 75–90.

Scheffer, M., Portielje, R., Zambrano, L., 2003. Fish facilitate wave resuspension of sediment. *Limnology and Oceanography*, 48(5), 1920–1926.

Simoes, F. d. S., Moreira, A. B., Bisinoti, M. C., Gimenez, S. M. N., Yabe, M. J. S., 2008. Water quality index as a simple indicator of aquaculture effects on aquatic bodies. *Ecological Indicators*, 8(5), 476–484.

Tamayo-Zafaralla, M., Santos, R. A. V., Orozco, R. P., Elegado, G. C. P., 2010. The ecological status of Lake Laguna de Bay, Philippines. *Aquatic Ecosystem Health Management*, 5(2), 127–138.

Uncles, R. J., Bloomer, N. J., Frickers, P. . E., Griffiths, M. L., Harris, C., Howland, R. J. M., Morris, A. W., Plummer, D. H., Tappin, A. D., 2017. Seasonal variability of salinity, temperature, turbidity and suspended chlorophyll in the Tweed Estuary. *Science of the Total Environment*, 55(6), 3501–3515.

Valipour, R., Boegman, L., Bouffard, D., Rao, Y. R., 2017. Sediment resuspension mechanisms and their contributions to high-turbidity events in a large lake. *Limnology and Oceanography*, 62(3), 1050–1067.

Vanhellemont, Q., Ruddick, K., 2014. Turbid wakes associated with offshore wind turbines observed with Landsat 8. *Remote Sensing of the Environment*, 145, 105–115.

Vanhellemont, Q., Ruddick, K., 2015. Advantages of high quality SWIR bands for ocean colour processing: Examples from Landsat-8. *Remote Sensing of the Environment*, 161, 89–106.

Yahel, R., Yahel, G., Genin, A., 2002. Daily cycles of suspended sand at coral reefs: A biological control. *Limnology and Oceanography*, 47(4), 1071–1083.